Check for updates

View Article Online
View Journal

Energy &
Environmental
Science

Accepted Manuscript

This article can be cited before page numbers have been issued, to do this please use: S. Cao, A. Zhang, H. Fang, B. Feng, Y. Liu, P. Yi, S. He, Z. Ren, L. Ma, W. Lu, M. Ye and J. Shen, *Energy Environ. Sci.*, 2025, DOI: 10.1039/D4EE05527F.

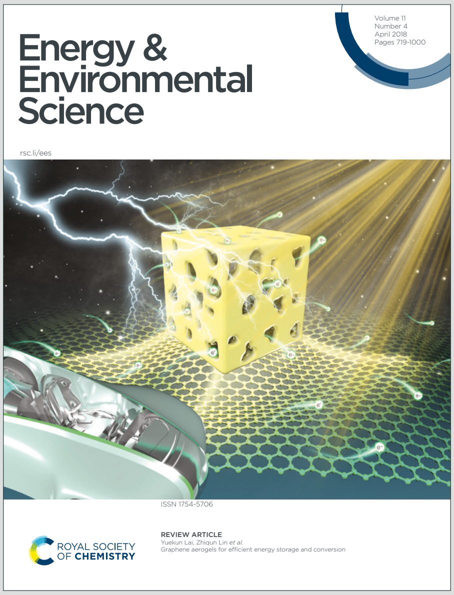

ROYAL SOCIETY
OF CHEMISTRY

rsc.li/ees

View Article Online
DOI: 10.1039/D4EE05527F

Skin-like quasi-solid-state electrolytes for spontaneous zinc-ion dehydration toward ultra-stable zinc-iodine batteries

Broader context

Aqueous zinc-iodine (Zn-I_2) batteries are potential alternatives to conventional lithium batteries due to their economic efficiency and sustainability. However, problems such as the shuttle effect of polyiodide and zinc anode side reactions lead to reduced battery lifetime. Here, a concept of a skin-like quasi-solid-state electrolyte (skin-QSSE) was proposed, which was composed using covalent organic framework (COF) nanolayers and aramid fiber hydrogel layers. This asymmetric structure presented the advantage of simultaneously dealing with the issues of iodine shuttling at the cathode and side reactions at the anode interface of Zn-I_2 batteries. This study provides new insights into solving the problem of aqueous zinc batteries from an asymmetric electrolyte perspective, with potential for other energy storage applications.

View Article Online
DOI: 10.1039/D4EE05527F

ARTICLE

Skin-like quasi-solid-state electrolytes for spontaneous zinc-ion dehydration toward ultra-stable zinc-iodine batteries

Received 00th January 20xx,
Accepted 00th January 20xx

DOI: 10.1039/x0xx00000x

Shaochong Cao,[a,b] Aiwen Zhang,[c] Huayi Fang,[d] Bingjian Feng,[d] Yongshuai Liu,[a,b] Pengshu Yi,[a,b] Shan He,[a,b] Zhouhong Ren,[a,b] Longli Ma,[a,b] Wenyi Lu,[a,b] Mingxin Ye,[a] and Jianfeng Shen*[a]

Rechargeable aqueous zinc-iodine (Zn-I_2) batteries are cost-effective alternative candidates for conventional metal-based batteries due to their sustainability in fabrication and source. However, the issues of the shuttle effect of polyiodides and Zn anode side reactions, are urgently addressed for large-scale energy storage applications. Here, we propose a biologically inspired concept of a skin-like quasi-solid-state electrolyte (skin-QSSE), which features an asymmetric structure composed of covalent organic framework (COF) nanolayers and aramid fiber hydrogel layers. The electrostatic repulsion between the negatively charged nitrogen sites on the triazine COF skeleton and the polyiodide ensures efficient utilization of the iodine-activated material. Notably, DFT calculations revealed that ANFs aramid fiber hydrogels induced a spontaneous dehydration process by lowering the desolvation energy barrier (-0.66 eV vs. 7.09 eV for liquid electrolyte) of hydrated zinc ions ($Zn(H_2O)_6^{2+}$), which alleviates corrosion and dendrite formation at the Zn anode interface. Ultimately, the Zn-I_2 batteries with the skin-QSSE demonstrated ultra-stable cycling reversibility with an extremely low capacity decay rate of only 0.0018‰ over 45000 cycles at 10 C. This work presents novel insights from the standpoint of asymmetric electrolytes for coping with the anode and cathode interface issues in aqueous Zn batteries.

Broader context

Aqueous zinc-iodine (Zn-I_2) batteries are potential alternatives to conventional lithium batteries due to their economic efficiency and sustainability. However, problems such as the shuttle effect of polyiodide and zinc anode side reactions lead to reduced battery lifetime. Here, a concept of a skin-like quasi-solid-state electrolyte (skin-QSSE) was proposed, which was composed using covalent organic framework (COF) nanolayers and aramid fiber hydrogel layers. This asymmetric structure presented the advantage of simultaneously dealing with the issues of iodine shuttling at the cathode and side reactions at the anode interface of Zn-I_2 batteries. This study provides new insights into solving the problem of aqueous zinc batteries from an asymmetric electrolyte perspective, with potential for other energy storage applications.

Introduction

Rechargeable aqueous batteries are regarded as encouraging next-generation commercially available battery systems owing to their inherent safety, less dependent on scarce resources, long-term stability, and non-toxicity.[1-7] Among the abundant aqueous batteries, rechargeable zinc-iodine (Zn-I_2) batteries have garnered considerable attention for their independence from scarce resources (55 μg L^{-1} iodine in the ocean and 0.075‰ Zn in the earth crust).[8-12] Different from Zn ion batteries with an intercalation/de-intercalation mechanism, the triiodide/iodide (I^-/I_3^-) redox couple of the iodine cathode is completely reversible, thus the Zn-I_2 battery provides a flat and stable charging/discharging plateau.[13, 14] However, highly soluble polyiodides are formed on the cathode side, which shuttle along a concentration gradient, leading to the irreversible loss of active materials.[15] Zn anode undergoes severe side reactions (e.g., hydrogen evolution reaction, iodine corrosion, and self-corrosion reaction) and severe dendrite growth, which shortens the lifespan of Zn-I_2 batteries.[16]

To tackle the above issues, numerous advanced strategies have been employed for iodine shuttle suppression and Zn cathode protection to facilitate the prolonged durability of the Zn-I_2 battery. A variety of functional cathode materials were created as hosts for iodine anchoring and confinement, including carbon-based materials,[17, 18] MXene,[14] and organic porous materials.[19-21] These materials suppress iodine shuttle via physical confinement or

---

[a] *S. C. Cao, Y. S. Liu, P. S. Yi, S. He, Z. H. Ren, L. L. Ma, W. Y. Lu, M. X. Ye, J. F. Shen*
Institute of Special Materials and Technology, Fudan University, Shanghai 200433, China. E-mail: jfshen@fudan.edu.cn
[b] *S. C. Cao, Y. S. Liu, P. S. Yi, S. He, Z. H. Ren, L. L. Ma, W. Y. Lu*
Department of Materials Science, Fudan University, Shanghai 200433, China
[c] *A. W. Zhang*
Department of Chemical Science and Engineering & Research Center for Membrane and Film Technology, Kobe University, Kobe, 657-8501 Japan
[d] *H. Y. Fang, B. J. Feng*
School of Materials Science and Engineering & Tianjin Key Lab for Rare Earth Materials and Applications, Nankai University, Tianjin 300350, P. R. China

Supplementary Information available: [details of any supplementary information available should be included here]. See DOI: 10.1039/x0xx00000x

View Article Online
DOI: 10.1039/D4EE05837E

chemisorption, yet fail to regulate Zn ions transportation. Some pioneer strategies of coating high-performance modification layers on Zn anodes or constructing alloy anodes have effectively modulated the Zn ion transfer and deposition behavior.[16, 22] However, simultaneous achievement of iodine cathode optimization and Zn anode protection is extremely tricky issue, since the aforementioned techniques are only partially functional. To date, a wide range of adaptable electrolytes, including functional additives,[23] deep eutectic electrolytes,[24] and asymmetric electrolytes,[25, 26] have been developed to address the issues with both cathode and anode interface. Among them, asymmetric electrolytes constructed from hydrogels are optimized for both the anode and cathode-electrolyte interfaces, due to the tunability of functional groups, flexibility, and water retention capacity.[25] Polyanionic hydrogel and polycationic hydrogel were connected to form a heterogeneous electrolyte, which was used to immobilize iodine species and regulate the uniform Zn deposition. Nevertheless, this emerging asymmetric design is still in its infancy, and the demand-driven design of novel electrolyte still requires further investigation.

Skin is a protective organ of the human body with brilliant structure and remarkable versatility.[27, 28] As shown in Scheme 1a, the outside layer of the asymmetric skin is a thin epidermis that prevents the invasion of bacteria and micro-organisms while not impeding gas and moisture exchange.[29] In addition, the interior of the skin features a hydrogel-like fiber network composed of dermis and hypodermis. Strong water retention, high elasticity, and toughness in the dermis and hypodermis help to prevent dehydration and dryness while also controlling metabolism.[30] This unique structure of the skin inspires us to prepare an asymmetric skin-like electrolyte for simultaneously regulating the interfaces of the anode and cathode in Zn-I_2 batteries. Aramid nanofiber (Protonated poly(*p*-phenylene terephthalamide), PPTA) hydrogel, with skin-like properties such as excellent water retention, high elasticity, and high flexibility, is a promising candidate for quasi-solid-state electrolyte (QSSE) of zinc-based batteries.[31] In 2023, Li et al. reported PPTA hydrogels have a rich fiber network that immobilizes anions, promotes uniform flow of Zn^{2+} ions, and attenuates the space-charge layer effect.[32] The amide groups (-CO-NH-) on the nanofiber network contribute to the regulation of hydrated zinc ions by hydrogen bonding (Scheme 1b, left).[32] Covalent organic frameworks (COFs) as porous crystalline polymers, have made significant advances in the field of selective separation.[33, 34] Therefore, fabricating functionalized COF nanolayers on the surface of PPTA hydrogel to selectively inhibit iodide ion penetration is a highly promising approach (Scheme 1b, right). Thus, asymmetric QSSE are obtained via integrating thin COF nanolayers onto the hydrogel, potentially advancing the development of long-life Zn-I_2 batteries.

Here, we propose a skin-like QSSE (skin-QSSE), obtained by incorporating triazine COF (TFB-TAPT) with abundant negatively charged N-sites onto aramid nanofiber hydrogels by *in situ* interfacial synthesis. Compared to the liquid electrolyte (LE, 2M $ZnSO_4$), the PPTA aramid fibers hydrogel reduced the energy barrier (-0.66 Ev vs. 7.09 eV for LE) for desolvation of hydrated Zn ions ($Zn(H_2O)_6^{2+}$) via the hydrogen bonding network, thereby mitigating corrosion of Zn anode. The amide groups (-CO-NH-) of the hydrogel fiber network ensured stable migration of Zn^{2+} along the hydrogel chain to avoid dendrite growth ($t_{Zn^{2+}}$=0.429 for skin-QSSE vs. 0.348 for LE). The Zn//Zn battery with skin-QSSE maintained a lower polarization voltage over 2490 cycles at 1 mA cm^{-2}, which indicated a stable Zn deposition/exfoliation process at the anode interface. More importantly, the electrostatic potential (ESP) map of TFB-TAPT showed a distinct negative charge accumulation at the nitrogen site, which endowed it with superior inhibition of polyiodide ions (I^- and I_3^- etc.) shuttling properties via electrostatic repulsion. As expected, skin-QSSE assembled Zn-I_2 full batteries demonstrated ultra-stability over 45000 cycles at 10 C, with an ultra-low decay rate of 0.0018‰ per cycle. Pouch Zn-I_2 batteries with skin-QSSE exhibited superior charge/discharge reversibility, and stabilized voltage even after bending and shearing, signifying their potential for practical applications. This study presents a concept of asymmetric skin-QSSE through bio-inspiration, which promises to simultaneously regulate the cathode and anode interfaces toward the ultra-stable aqueous battery.

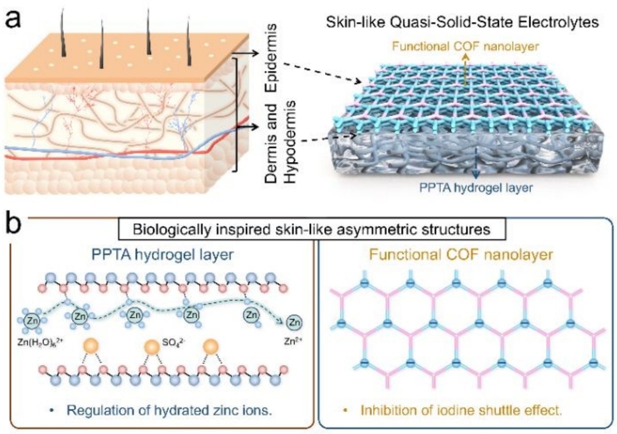

Scheme 1. (a) Schematic diagram of human skin and the skin-QSSE. (b) Regulation of the anode and cathode interfaces of Zn-I_2 batteries by asymmetric skin-QSSE.

Results and Discussion

Design of the Skin-QSSE

The concept of an asymmetric skin-QSSE assembled by triazine COF (TFB-TAPT) and PPTA hydrogel has been proposed to enhance the performance of Zn-I_2 batteries. TFB-TAPT is a microporous COF with an appropriate pore size (14 Å) and negatively charged triazine groups that effectively hinder iodide ion shuttling.[35] Furthermore, it is covalently linked through Schiff base reactions, providing high chemical stability to ensure the long lifespan of the battery. The interface compatibility between the COF nanolayers and the gel layer is a crucial consideration. PPTA hydrogel was used as a support template to synthesize polymer films due to its high mechanical properties, excellent hydrophilicity, high water content, and smooth surface.[36] PPTA hydrogels resemble a free aqueous phase, which

View Article Online
DOI: 10.1039/D4EE05527F

promotes a uniform interfacial polymerization reaction to obtain defect-free COF nanolayers.

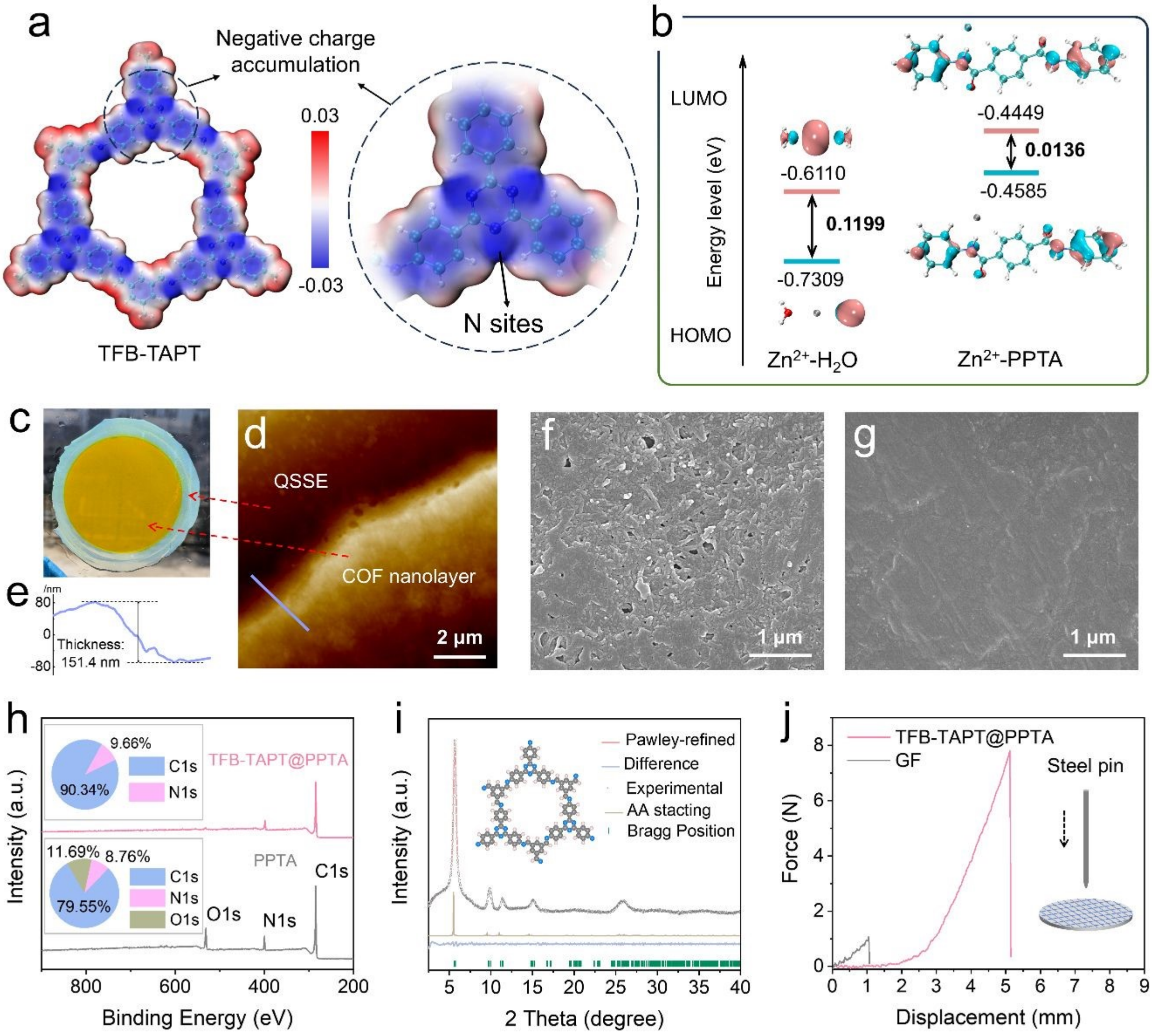

Figure 1. Properties of the skin-QSSE. (a) Electrostatic potential (ESP) distributions of TFB-TAPT. (b) Lowest unoccupied molecular orbital (LUMO) and the highest occupied molecular orbital (HOMO) of Zn^{2+}-H_2O (left) and Zn^{2+}-PPTA (right) complexes. (c) Digital photographs of the skin-like QSSE. AFM image (d) and COF layer thickness curve (e) of the skin-like QSSE. SEM images of the (f) QSSE and (g) skin-QSSE surface. (h) Wide-scan XPS spectra of PPTA and TFB-TAPT@PPTA surface (inset: elemental compositions). (i) Powder X-ray diffraction patterns of TFB-TAPT (inset: the chemical structure of TFB-TAPT). (j) Penetration force-displacement curves (inset: testing schematics) of TFB-TAPT@PPTA and glass fiber (GF).

Density functional theory (DFT) calculations were utilized to verify the structural and functional rationality of the skin-QSSE. As shown in Figure 1a, the electrostatic potential (ESP) distributions of TFB-TAPT displayed obvious aggregation (blue color region) of negative charges at the N site in the framework. This potentially inhibits the shuttle effect of negatively charged iodide ions (I^-/I_3^-) and promotes uniform transport of Zn^{2+} ionic flow through electrostatic interactions. The molecular orbital level was further investigated for the electron filling and extraction capacity, which responds to the activity of the redox reactions. The high highest occupied molecular orbital (HOMO) energy level endows PPTA with the ability to strongly coordinate with Zn^{2+} and remove water from the inner solvation shell, thus mitigating the corrosion of the Zn anode (Figure 1b).[37] Moreover, Zn^{2+}-PPTA exhibited the narrowest band gap (0.0136 Hartree) indicating improved electronic conductivity.[38] The above calculations signify the potential of the proposed skin-QSSE to address the diverse issues of the anode and cathode of Zn-I_2 batteries.

The skin-QSSE was prepared by two stages, namely the preparation of PPTA hydrogels by phase inversion and *in situ* interfacial synthesis of COF nanolayers. PPTA fibers with amide groups (-CO-NH-) undergo a deprotonation process in an alkaline environment, where the hydrogen bonding network is broken between the fiber chains (Figure S1). Water molecules act as proton donors to induce the re-protonation of PPTA to form hydrogels with fiber networks. Hydrophobic regions were constructed on the PPTA hydrogel surface to form an interface for the synthesis of thin triazine COF nanolayers (Figure S2). Specifically, aldehyde monomer (1,3,5-triformylbenzene (TFB) and amine monomer (4,4',4''-(1,3,5-triazine-2,4,6-triyl)trianiline, TAPT) were dispersed in the hydrophobic region

View Article Online
DOI: 10.1039/D4EE05527F

and hydrogel region, respectively, and acetic acid was utilized to initiate the Schiff base reaction at interface.[39] Finally, the obtained asymmetric TFB-TAPT@PPTA hydrogel was immersed in $ZnSO_4$ electrolyte diffused under a concentration gradient to acquire skin-QSSE.

Characterizations of the Skin-QSSE

Skin-QSSE showed an asymmetric structure of yellow COF cortex overlying the original transparent hydrogel (Figure 1c). The thickness of Skin-QSSE was 170 μm, which is thinner than commercial glass fiber (GF) separator (960 μm), shortening the ion transfer distance (Figure S3). The thickness of the TFB-TAPT nanolayer was further verified at the skin-QSSE boundary using atomic force microscopy (AFM), as shown in Figure 1d. The thickness profile analysis revealed the thickness of the COF nanolayer covering the hydrogel surface to be 151.4 nm (Figure 1e). The surface morphology of PPTA QSSE without COF nanolayer was observed by scanning electron microscopy (SEM), which exhibited a porous nanofiber network structure as shown in Figure 1f. Upon *in-situ* synthesis of TFB-TAPT, the surface of the skin-QSSE displayed a continuous, uniform, and defect-free morphology (Figure 1g). The cross-sectional SEM image of skin-QSSE revealed an asymmetric structure consisting of thin TFB-TAPT nanolayers (~150 nm consistent with AFM thickness analysis) and nanofiber networks (Figure S4).

The chemical structure and elemental compositions of TFB-TAPT@PPTA were confirmed by X-ray photoelectron spectroscopy (XPS). Wide-scan XPS spectra of PPTA and TFB-TAPT@PPTA surface demonstrated the elements C, N, and O in 79.55%, 11.69%, and 8.76%, respectively (Figure 1h). It is noteworthy that the wide-scan XPS spectrum of the PPTA surface showed only C and N elements, consistent with the chemical structure of the COF, indicating the successful loading of the TFB-TAPT nanolayer. Imine-N appeared in the XPS spectrum of N 1s for imine-linked TFB-TAPT, implying the occurrence of Schiff base reaction (Figure S5). X-ray diffraction (XRD) patterns showed that the PPTA hydrogel films were amorphous polymers. The XRD pattern of TFB-TAPT@PPTA revealed a sharp peak

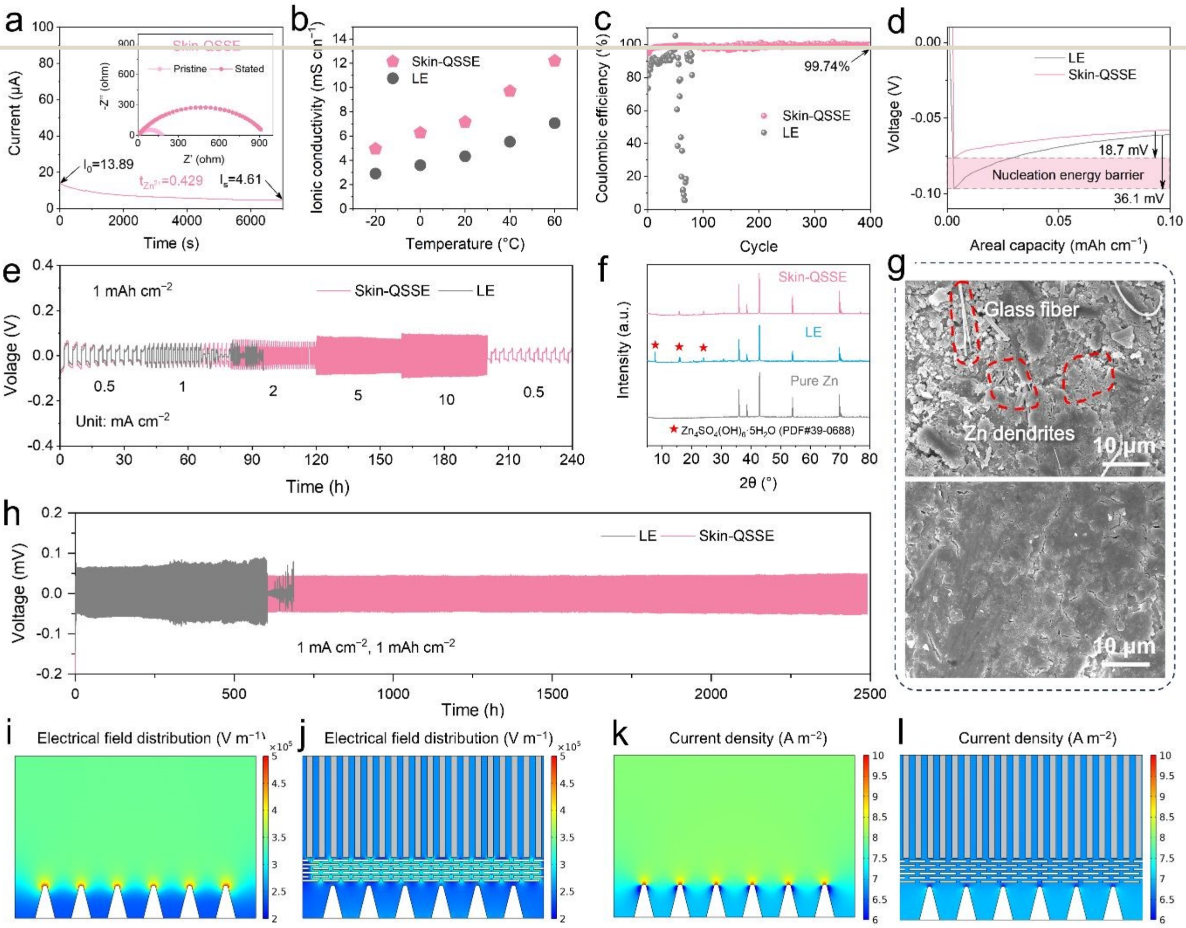

Figure 2. Electrochemical Performance of Symmetric Batteries with the skin-QSSE. (a) Nyquist plots and chronopotentiometric curve of the Zn//Zn symmetric batteries before and after polarization (ΔV=10 mV) and Zn^{2+} transference numbers in the skin-QSSE. (b) Ionic conductivity of LE and skin-QSSE at different temperatures (60% humidity). (c) Coulombic efficiencies of Zn//Cu batteries with skin-QSSE and LE at 1 mA cm^{-2} (0.5 mAh cm^{-2}). (d) Nucleation overpotentials using Zn//Cu batteries in LE and skin-QSSE (at 0.5 mA cm^{-2}). (e) Rate performance of Zn symmetric batteries with LE and skin-QSSE at different current densities. (f) XRD patterns of pristine Zn foils and Zn anodes after 100 h of Zn symmetric batteries with LE and skin-QSSE at 1 mA cm^{-2}. (g) SEM images of the anodes surface with LE (up) and skin-QSSE (down). (h) Cycling performance of Zn//Zn symmetric batteries with LE and skin-QSSE at 1 mA cm^{-2} (1 mAh cm^{-2}). COMSOL simulations of electric field distribution in (i) LE and (j) skin-QSSE. COMSOL simulations of current density distribution in (k) LE and (l) skin-QSSE.

View Article Online
DOI: 10.1039/D4EE05627F

at 5.8°, affiliating to (100) facet of TFB-TAPT (Figure S6).[40] However, the XRD characteristic peaks of TFB-TAPT in TFB-TAPT@PPTA were weak and probably affected by the peaks of PPTA. The free-standing TFB-TAPT nanofilms were prepared at the water-organic phase interface to further investigate the structure of the TFB-TAPT nanolayers. XRD pattern of TFB-TAPT indicated distinct peaks at 5.5° and 9.6°, matching well with the simulated PXRD pattern of the eclipsed (AA) stacking modes (Figure 1i).[41] The AA stacking implies the formation of an ordered crystal framework favoring ion transfer.

Fourier transform infrared (FT-IR) also provided reliable evidence for the formation of TFB-TAPT. The aldehyde monomer TFB and the amine monomer TAPT show stretching vibration peaks for -CHO (1700 cm^{-1}) and -N-H (3210 and 3320 cm^{-1}), respectively (Figure S7).[42] The monomer characteristic peaks were significantly weakened after the condensation reaction, implying a high degree of polymerization. The emerging peak of imine-linked TFB-TAPT at 1660 cm^{-1} was attributed to characteristic stretching band of C=N. Thanks to the intrinsic strong tensile strength and high modulus properties of PPTA nanofiber networks, TFB-TAPT@PPTA features excellent mechanical properties.[31] TFB-TAPT@PPTA demonstrated a significantly higher ultimate tensile strength of 5.5 MPa, in contrast to the GF (0.2 MPa) separator commonly used in aqueous Zn-ion batteries (Figure S8). In addition, puncture strength is also a critical property for solid electrolytes and separators to resist anode dendrites. As shown in Figure 1j, the puncture strength of TFB-TAPT@PPTA was nearly 8 times that of the GF separator, demonstrating significant potential for the physical inhibition of dendrite formation.

Electrochemical Performance of Symmetric Batteries with the Skin-QSSE

Various electrochemical studies were carried out to evaluate the performance of the skin-QSSE. The resistance of Zn//Zn symmetrical batteries with LE and skin-QSSE was surveyed by electrochemical impedance spectra (EIS). As illustrated in Figure S9, the skin-QSSE demonstrated significantly lower charge-transfer resistance compared to the LE. This decrease in resistance is likely due to the PPTA hydrogel fiber network, which provides abundant ion transport sites.[32] Zn^{2+} transference number and ionic conductivity were calculated to evaluate the ion transfer behavior within the skin-QSSE in depth. The Zn^{2+} transference number was obtained for the Zn//Zn symmetrical battery assembled with the skin-QSSE at a polarization potential of 10 mV. The Zn^{2+} transference number for the Zn//Zn symmetrical battery based on the skin-QSSE was calculated to be 0.429, which is higher than that of LE, indicating faster Zn^{2+} transfer in the skin-QSSE (Figure 2a and S10). Ionic conductivity is also a critical parameter to estimate the Zn^{2+} transport kinetics in the design of skin-QSSEs. Environmental factors, such as temperature and humidity, have a significant impact on the ion transport in hydrogels.[43] Firstly, the skin-QSSE was directly exposed to the environment to evaluate its water retention and ionic conductivity. The results showed that the water content of the skin-QSSE was reduced from the initial 95.8% to 90.3% and the ionic conductivity was only slightly reduced (from 10.8 to 10.3 mS cm^{-1}) after 72 h treatment at 20°C and 90% RH (Figure S11). In practical applications, skin-QSSE is typically enclosed within the battery, so its performance requires further consideration. As shown in Figure 2b, the ionic conductivity of skin-QSSE gradually increases with increasing temperature. In the range of -20°C to 60°C, the ionic conductivity of skin-QSSE was higher than that of LE, which implies a lower voltage polarization or overpotential for Zn deposition.[44]

The effect of the electrolyte on the stability and reversibility of Zn deposition and stripping was further investigated by carrying out the Coulombic efficiency (CE) of Zn//Cu batteries. As shown in Fig. 2c, the Zn//Cu battery with LE exhibited significant fluctuations within 100 cycles, while the CE of the battery assembled by skin-QSSE after 400 cycles was up to 99.74% (1 mA cm^{-2}), implying a uniform, reversible and stable Zn deposition/exfoliation process (Figure 2c). It was evident that the Zn//Cu batteries with the skin-QSSE exhibited significantly lower voltage polarization compared to those with the LE, indicating a lower energy barrier for Zn deposition (Figure S12). Furthermore, according to initial cycle of CE test, the skin-QSSE reduced the nucleation energy barrier to 18.7 mV, compared to 36.1 mV for the Zn//Cu batteries with LE (Figure 2d). The rate performance of the Zn//Zn symmetric batteries with LE and skin-QSSE for a fixed area capacity of 1 mAh cm^{-2} in the current density range of 0.5-10 mA cm^{-2} was presented in Figure 2e. The cycling performance of the Zn//Zn symmetric batteries with skin-QSSE were more stable with increasing current density, whereas the LE-assembled battery showed an internal short circuit at 1 mA cm^{-2}. Cyclic performance of Zn plating/stripping processes of Zn anodes with LE and Skin-QSSE were presented in Figure 2h. As expected, Zn//Zn batteries with the skin-QSSE demonstrated a 2490 h cycling life at 1 mA cm^{-2}, which was significantly longer than the batteries with the LE. This indicated that the nano-fiber network of the skin-QSSE induced uniform Zn^{2+} transfer, deposition, and stripping, thereby reducing dendrite growth on anodes surface. Notably, the Zn//Zn batteries with skin-QSSE at high current densities (5 mA cm^{-2}) displayed a steady cycling of 600 h and a low voltage polarization (Figure S13).

The microscopic morphology of the Zn deposition/exfoliation process on the anode surface urgently requires in-depth investigation to analyze the failure mechanism. The XRD patterns indicated obvious diffraction peaks of by-products of basic Zn sulfate ($Zn_4(OH)_6SO_4\square 5H_2O$) after 100 h cycling using LE (Figure 2f).[16, 22] However, the characteristic peaks on the anode surface under the influence of the skin-QSSE significantly weakened, indicating that the skin-QSSE mitigated Zn corrosion by the suppression of SO_4^{2-} migration.[45] SEM images verified that severe corrosion and dendrite growth were produced at the Zn anode surface using LE (Figure 2g). Conversely, the surface of the Zn foil after 100 h deposition with skin-QSSE was flat and smooth, confirming that skin-QSSE promotes uniform Zn deposition and exfoliation.

Mechanism Investigation for the Skin-QSSE.

Based on the Finite element method (FEM), a micro zone model was established to analyze the electric field distribution, current density distribution and concentration field by COMSOL Multiphysics.[46] The asymmetric Skin-QSSE was simplified to a bilayer structure containing a gel layer and a porous channel layer. However, the high ionic conductivity based on skin-QSSE produced a uniform electric field and current density distribution that guided uniform and rapid Zn deposition and stripping (Figure 2j and 2l). In addition, the Zn^{2+} concentration field confirmed that, the skin-QSSE facilitated

View Article Online
DOI: 10.1039/D4EE05527F

a more uniform Zn ion flux compared to that in the LE (Figure S14). The results of COMSOL simulations implied that the ordered COF nano-channels and aramid fibers acted as ion pumps to optimize the ion diffusion kinetics and reduce the concentration polarization at the anode interface.

Theoretical calculations and simulations were utilized to further analyze the special mechanism of the COF nanolayer and PPTA hydrogel layer within the asymmetric skin-QSSE. Microscopic solvated structures on the electrode-electrolyte phase interface were investigated at the molecular/atomic level using density functional theory (DFT). Based on binding energy calculations, the interactions between the PPTA aramid fiber chain and SO_4^{2-} (ΔE= -57.7 kJ mol^{-1}) are stronger than those with $Zn(H_2O)_5^{2+}$ (ΔE= -20.5 kJ mol^{-1}), indicating a powerful obstruction to SO_4^{2-} diffusion (Figure 3a and S19). According to Sand's model, as Zn deposition proceeds, the continuous reduction in salt concentration near the Zn anode leads to strong space charge effects, causing severe dendrite formation (Figure 3b).[47] Compared to the LE environment, the concentration polarization at the anode-electrolyte interface was attenuated due to the immobilization of SO_4^{2-} anions by PPTA, thus mitigating the growth of dendrites.

In aqueous electrolytes, Zn^{2+} are surrounded by water molecules to form solvated Zn^{2+}, which are associated closely with Zn passivation caused by side reactions and corrosion.[48] Reducing the content of solvated $[Zn(H_2O)_6]^{2+}$ and controlling the formation of active free water near the Zn anode are effective strategies to enhance the corrosion resistance of Zn foil. For the LE, the desolvation energies of hydrated Zn^{2+} for the dehydration process continuously increased, with the barrier reaching up to 7.09 eV from $Zn(H_2O)_6^{2+}$ to Zn^{2+}, as shown in Figure 3c and S16. In contrast, the amide (-CO-NH-) groups on the PPTA molecular chain are capable of lowering the desolvation energies during the Zn deposition process. Limited by the spatial steric hindrance of the PPTA molecular chain, Zn ions can maximally coordinate with four PPTA molecules. As depicted in Figure 3c and S17, the desolvation energies gradually decreased with the introduction of:

PPTA ($Zn(H_2O)_6^{2+}$→$Zn(H_2O)_5(PPTA)^{2+}$: -0.15 eV;
$Zn(H_2O)_5(PPTA)^{2+}$→$Zn(H_2O)_4(PPTA)_2^{2+}$: -0.43 eV;
$Zn(H_2O)_4(PPTA)_2^{2+}$→$Zn(H_2O)_3(PPTA)_3^{2+}$: -1.00 eV;
$Zn(H_2O)_3(PPTA)_3^{2+}$→$Zn(H_2O)_2(PPTA)_4^{2+}$: -0.40 eV.

The desolvation energy from $Zn(H_2O)_6^{2+}$ to Zn^{2+} influenced by PPTA is -0.66 eV, which implies that the $Zn(H_2O)_6^{2+}$ was endowed with the ability of spontaneous dehydration in skin-QSSE. In addition, only one PPTA was controlled to coordinate with the Zn^{2+} to further understand the ability of PPTA to reduce the desolvation energy (Figure S18). Despite only a single PPTA molecule coordinating with Zn^{2+}, the energy barrier for each step of the dehydration reaction was significantly reduced compared to the LE (without PPTA). The facile

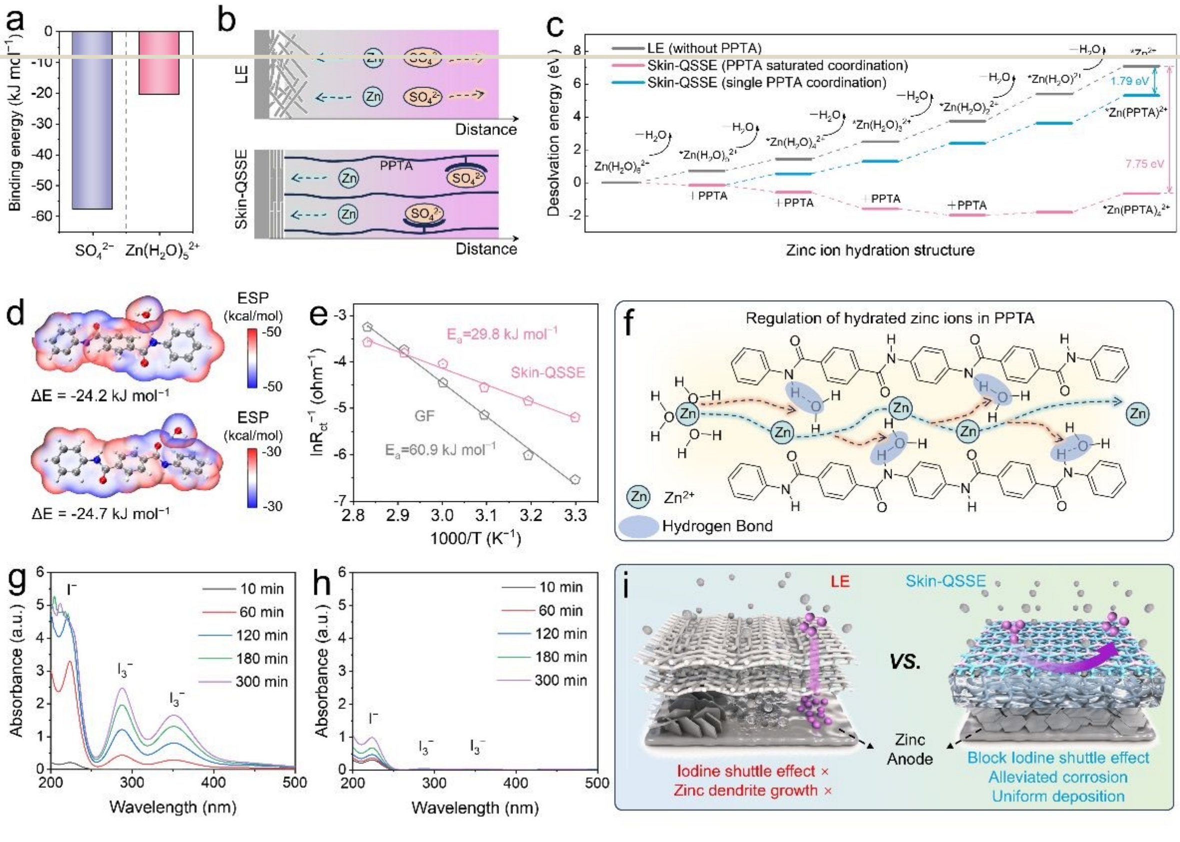

Figure 3. Theoretical calculation and mechanism investigation for the skin-QSSE. (a) Binding energies of SO_4^{2-} and $Zn(H_2O)_5^{2+}$ on PPTA. (b) Migration behavior of Zn ions and SO_4^{2-} in different electrolytes. (c) Desolvation energies for the removal of H_2O molecules on $Zn(H_2O)_6^{2+}$ in LE (without PPTA) and skin-QSSE (with PPTA). (d) Binding energies and ESP distributions of H_2O on the amide groups (-CO-NH-) of PPTA. (e) Arrhenius curves and desolvation activation energies (E_a) of LE and skin-QSEE. (f) Schematic illustration of the migration of hydrated Zn^{2+} inside skin-QSSE nanofibers. UV-Vis absorption spectra of the right chamber of H-type glass cell with (g) LE and (h) skin-QSSE. (i) Mechanism diagram of skin-QSSE for both anode and cathode regulation.

View Article Online
DOI: 10.1039/D4EE05527F

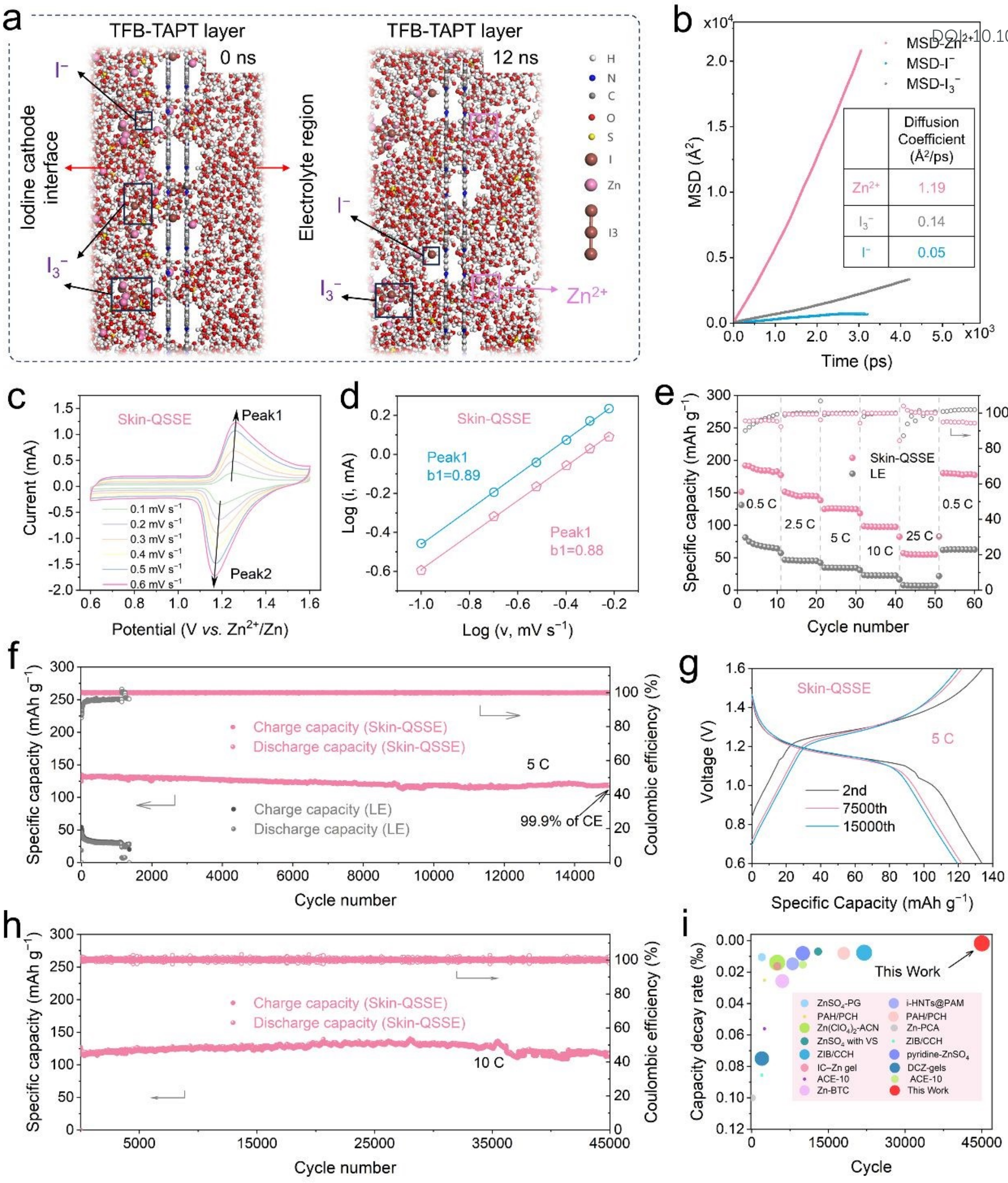

Figure 4. Performance Evaluation of Zn-I$_2$ Batteries with the skin-QSSE. (a) The snapshot extracted from the MD simulations of the ion transport behavior in TFB-TAPT nanolayers at 0 ns (left), 12 ns (right). The white atoms are H, blue atoms are N, grey atoms are C, red atoms are O, yellow atoms are S, brown atoms are I and pink atoms are Zn. (b) Time-dependent mean squared displacements (MSDs) of ions in TFB-TAPT. (c) The cyclic voltammetry (CV) curves and (d) log-linear relationship of oxidation and reduction peak currents versus scan rates of Zn-I$_2$ batteries with skin-QSSE at different scan rates. (e) Rate performance of Zn-I$_2$ batteries with LE and skin-QSSE at different C-rates. (f) Long-term cycling performance for Zn-I$_2$ batteries with LE and skin-QSSE at 5 C (1 C = 0.211 A g^{-1}). (g) The galvanostatic charge-discharge (GCD) curves of the Zn-I$_2$ batteries assembled by QSSE and LE at 5 C. (h) Long-term cycling performance for Zn-I$_2$ batteries with skin-QSSE at 10 C. (i) Comparison of cycling and capacity decay rate performance over other advanced Zn-I$_2$ batteries (circle diameter represents C-rates, see Table S1 for detailed parameters).

desolvation procedure initiated by PPTA is pivotal for the mitigation of dendrite growth and side reactions at the electrode-electrolyte interface. The binding energies of -24.2 and -24.7 kJ mol^{-1} between the N and O sites on the amide bonds of the PPTA molecular chain and water molecules suggest that PPTA might lower the Zn desolvation energy by capturing water through hydrogen bonding (Figure 3d). Additionally, the desolvation activation energy (E_a) in the skin-QSSE was calculated from the Arrhenius curves to be 29.8 kJ mol^{-1}, which was nearly half that of the LE (60.9 kJ mol^{-1}), consistent with the DFT calculation results (Figure 3e and S15). Consequently, the migration behavior of hydrated Zn^{2+} within PPTA nanofibers is illustrated schematically in Figure 3f. As hydrated Zn^{2+} approach the PPTA fibers, water molecules are trapped by hydrogen bonding

View Article Online
DOI: 10.1039/D4EE05527E

interaction with the amide bonds, allowing the Zn^{2+} to rapidly transfer along the nanofiber network.

The study mentioned above proved that the skin-QSSE are favorable for the Zn anode regulation, but the effect of TFB-TAPT nanolayers on the behavior of the iodine shuttle effect was also require to be evaluated. The diffusion control contrast of electrolytes on polyiodides was undertaken by a visual diffusion change. Clearly, the GF started diffusion of iodide ions within 10 min, and the right chamber turned brownish at 300 min, indicating a significant amount of I_3^- shuttling (Figure S20). As shown in Figure 3g, the UV-visible spectrum of the permeate displayed distinct I^- and I_3^- characteristic peaks. In contrast, UV-visible spectroscopy justified the effective shuttle control of iodide ion by the skin-QSSE, as no characteristic peaks of I_3^- were observed in the permeate solution (Figure 3h). On the back side of the skin-QSSE, no characteristic peaks of iodide ions were observed in the XPS spectra after the visual shuttle experiment (Figure S21). In addition, QSSE without TFB-TAPT nanolayers failed to control iodide ion shuttle significantly, implying that TFB-TAPT nanolayers in the asymmetric skin-QSSE played a crucial role of diffusion inhibition (Figure S22). Zeta potentials revealed that PPTA hydrogels loaded with TFB-TAPT exhibited low negative charges over a wide pH range (Figure S23). Therefore, the control of iodide ion shuttling was primarily governed by electrostatic repulsion of the negatively charged backbone on the TFB-TAPT. The mechanism of optimization for the Zn deposition process and the iodide shuttle suppression by the asymmetric skin-QSSE, composed of TFB-TAPT and PPTA hydrogel, is illustrated in Figure 3i. Effective iodine-selective blocking was provided by the TFB-TAPT nanolayer via electrostatic repulsion. The PPTA hydrogel mitigates Zn foil corrosion and alleviates dendrite growth by regulating the migration behavior of hydrated Zn^{2+} and SO_4^{2-}.

To evaluate the effect of TFB-TAPT on the ion diffusion behavior in skin-QSSE, MD simulations were performed to visualize ion diffusion and quantify the diffusion rate. A diffusion model containing two layers of TFB-TAPT was established to simulate the iodide cathode interface, including 88 SO_4^{2-}, 88 Zn^{2+}, 16 I^-, 16 I_3^-, and 1800 H_2O molecules. Figure 4a shows a snapshot of the MD simulation configuration at 0 ns, where iodide ions and $ZnSO_4$ are concentrated on the left side of the COF layer. Obviously, as random configuration proceeds to 12 ns, Zn^{2+} predominantly enter the TFB-TAPT and diffuse to the right side, while polyiodide ion anions are selectively blocked by the COF layer. The diffusion coefficients of various ions were quantified by mean squared displacements (MSD) versus time curves. In the TFB-TAPT nanochannels, the diffusion coefficient of Zn^{2+} was as high as 1.19 $Å^2$ ps^{-1}, which is significantly higher than the diffusion coefficients of I_3^- (0.14 $Å^2$ ps^{-1}) and I^- (0.05 $Å^2$ ps^{-1}) ions (Figure 4b). As illustrated in Figure S24, the Radial distribution functions (RDFs) of Zn^{2+}, I^- and I_3^- for the triazine groups on the TFB-TAPT skeleton were calculated. In contrast to Zn^{2+}, the RDF peaks of I^- and I_3^- are more prominent, suggesting strong interaction with TFB-TAPT leading to blocked diffusion.

Performance Evaluation of Zn-I_2 Batteries with the Skin-QSSE

The Zn-I_2 full battery was assembled to demonstrate the electrochemical performance of the asymmetric skin-QSSE. An iodine cathode was constructed using active carbon (AC) as the host. The BET specific surface area of I_2@AC decreased significantly, proving that iodine occupied the pores of the AC, confirming the successful loading of iodine (Figure S25). The iodine loading of the active materials in cathode was determined by thermogravimetric analysis (TGA, Figure S26). The cyclic voltammetry (CV) curves displayed a pair of oxidation-reduction peaks corresponding to the typical two-electron reaction between I_2 and I^-/I_3^- (Figure S27). The lower potential difference between the redox peaks and larger current of skin-QSSE compared to LE implied low polarization and remarkable redox kinetics.[49] The voltage gap between the reduction and oxidation peaks gradually widened when the scan rate ranged from 0.1 to 0.6 mV s^{-1} (Figure 4c, S28). Log-linear relationship between the peak current values and scan rate was obtained according to the equation $i = a\ v^b$ as illustrated in Figure 4d. The calculated anodic peak and cathodic peak b values were 0.89 and 0.88 for skin-QSSE and LE, respectively, both falling within the range of 0.5-1. This suggests that the electrochemical reaction for Zn-I_2 battery is jointly controlled by ion diffusion and pseudocapacitance.[50]

The rate performance of full-batteries at different C-rates was used to fully evaluate the benefits of skin-QSSE for LE. Across the range of 0.5 C to 25 C rates, full batteries equipped with skin-QSSE exhibited consistently superior specific capacities (Figure 4e). Even when the C-rate decreases from 25 to 0.5 C, the specific capacity recovers to 190.1 mAh g^{-1}, demonstrating high reversibility. Furthermore, the flat discharge voltage platform for skin-QSSE at high C-rates from the GCD curves meant fast electrochemical reaction kinetics (Figure S29).[51] A full battery assembled using QSSE without the TFB-TAPT nanolayer was employed to further analyze the role of asymmetric skin-QSSE bilayer structure (Figure S30). The specific capacity of the Zn-I_2 batteries without TFB-TAPT was decreased compared to batteries utilizing skin-QSSE, due to the dominant role of the COF nanolayer in the inhibition of iodide ion shuttling.

Due to the skin-QSSE promoting uniform Zn plating/stripping and inhibiting iodine shuttle, the assembled Zn-I_2 battery demonstrates ultra-stable long-term cycling performance. As presented in Figure S31, the initial specific capacity of the skin-QSSE-assembled battery as high as 201.5 mAh g^{-1} at 0.5 C, which is approaching the theoretical capacity (211 mAh g^{-1}).[52] At high C-rates (5 C), 99.9% Coulomb efficiency (CE) is still guaranteed and the capacity decay rate calculated to be 0.0072‰ after 15000 cycles (Figure 4f) for the skin-QSSE. Notably, quite stable charging/discharging plateaus were maintained at 7500th and 15000th cycles, which were revealed from the GCD curves (Figure 4g). In contrast, Zn-I_2 batteries with LE exhibited lower initial capacity and significant capacity decay within 1300 cycles due to excessive iodine shuttle. Comparative analysis of previously reported Zn-I_2 batteries based on separator and electrolyte demonstrated the superior performance of our designed asymmetric skin-QSSE (Figure 4i, see Table S1 for detailed parameters). Specifically, Zn-I_2 batteries with skin-QSSE in our work demonstrated an ultra-stable cycling performance, with a capacity decay rate of only 0.0018‰ over 45000 cycles at 10 C, which is superior to the reported state-of-the-art Zn-I_2 batteries (Figure 4h).

Post-cycling skin-QSSE was systematically characterized to verify its integrity and structural stability under repeated charge/discharge process. Optical image of skin-QSSE after 100 h cycling indicates that

View Article Online
DOI: 10.1039/D4EE05527F

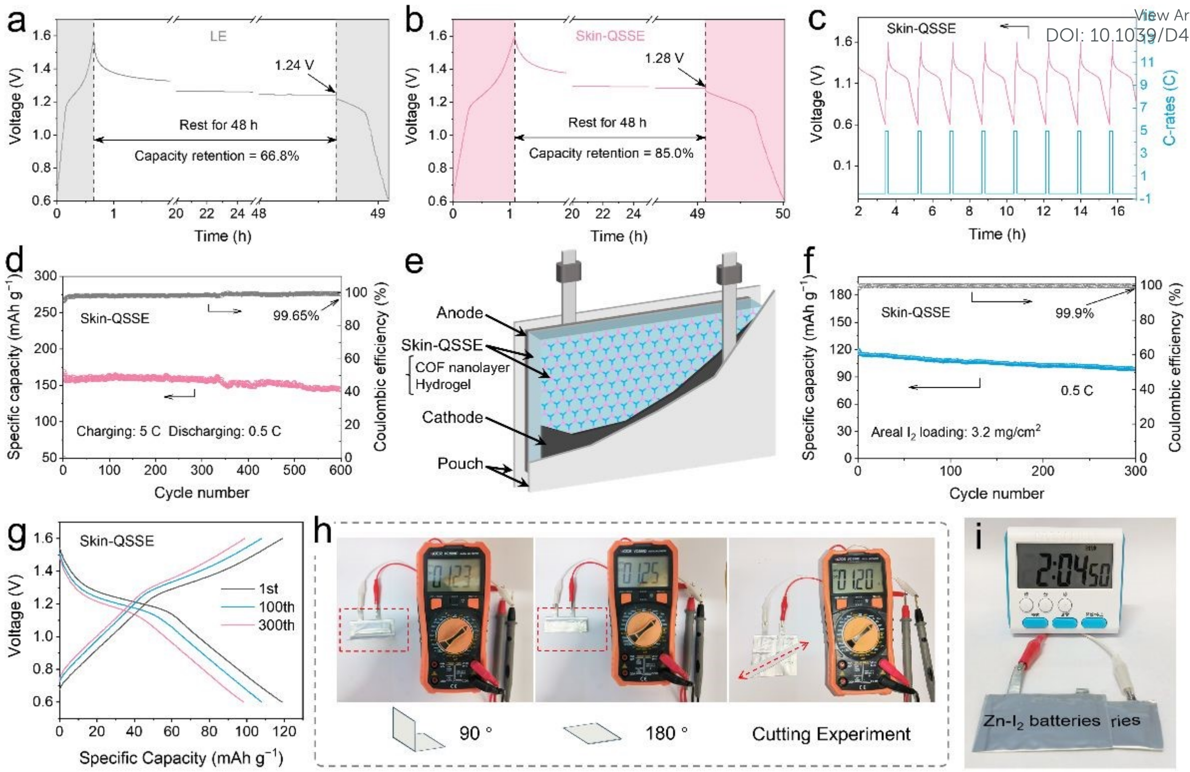

Figure 5. Performance of the Zn-I$_2$ pouch batteries. Self-discharge performance of the Zn-I$_2$ batteries with (a) LE and (b) skin-QSSE. (c) The voltage-time curves of fast-charging and slow-discharging process. (d) Fast-charging and slow-discharging cycle performance of the Zn-I$_2$ batteries assembled by skin-QSSE. (e) Schematic diagram of the Zn-I$_2$ pouch batteries with skin-QSSE. (f) Cycling performance of the Zn-I$_2$ batteries with skin-QSSE and (g) the galvanostatic charge–discharge (GCD) curves (1 × 2 cm^2 of iodine cathode). (h) Bending and cutting experiments on the Zn-I$_2$ pouch batteries. (i) Optical photograph of pouch batteries with skin-QSSE in series power a timer.

retains its integrity (Inset of the Figure S32). SEM images reveal that the skin-QSSE maintains its surface structure without visible cracks, indicating robust mechanical integrity after prolonged cycling (Figure S32). FT-IR and XPS analyses of post-cycling skin-QSSE were performed to evaluate the structural stability and potential degradation risks. The characteristic peaks at 1642 and 1540 cm^{-1} of used skin-QSSE are attributed to the stretching vibration of -C═O, along with the coupled -N-H bending signal and -C-N stretching vibration (Figure S33).[53] This indicates that the amide bonds (-C=O-NH-) of PPTA are still present after cycling, demonstrating its excellent structural stability.

XPS was used to further investigate the structural changes of the asymmetric skin-QSSE on the COF side and PPTA side before and after cycling. PPTA side faces the Zn anode, undergoing issues such as dendrite growth and corrosion at the anode interface. The high-resolution XPS spectra of the PPTA side of the used skin-QSSE were consistent with that of the initial skin-QSSE, with no formation or disappearance of chemical bonds (Figure S34). This suggests that the amide-linked PPTA provides high electrochemical stability.

For the COF side, the TFB-TAPT nanolayer suppresses iodine shuttling at the cathodic interface. Notably, the high-resolution N 1s spectrum shows a new peak at 401.7 eV, which is attributed to the N-I species (Figure S35).[54, 55] This is due to the interaction of I$^-$ with the TFB-TAPT nanolayer, where the I$^-$ anion bonds the N by an ionic bond.[56] In addition, the characteristic peak of the C=N bond for the TFB-TAPT is evident at 398.7 eV, confirming the high chemical stability of imine-linked COFs in charge/discharge cycle.

More importantly, fast self-discharge deriving from cross-migration of soluble polyiodides in aqueous media for Zn-I$_2$ batteries, ultimately leading to low specific capacity and reduced Coulombic efficiency.[57] As depicted in Figure 5a, the batteries using LE retained only 66.8% of its initial capacity after 48 h of resting. Thanks to the excellent suppression of iodide ion shuttling by TFB-TAPT nanolayers, the capacity retention of skin-QSSE-assembled batteries was enhanced to 85.0% after 48 h resting (Figure 5b). The rapid advancement of electronic devices has underscored the urgent requirement for secondary batteries capable of fast-charging and slow-discharging. The Zn-I$_2$ batteries with skin-QSSE display a distinct discharge voltage plateau at a high charging rate of 5 C and a low discharge rate of 0.5 C condition (Figure 5c). As depicted in Figure 5d, the battery demonstrates a high initial specific capacity of 164.6 mAh g^{-1} and maintains stable CE (99.7% at the 600th cycle). Additionally, the GCD curves revealed that flat discharging plateaus were maintained at 2nd, 100th, 300th and 600th cycles, indicating stable Zn ions transport in term of fast-charging-slow-discharging process (Figure S36).

Taking advantage of the flexibility of ANF hydrogels, Zn-I$_2$ pouch batteries were assembled with multiple layers of Zn foil, skin-QSSE, and iodine cathode to explore their practical application, as depicted in Figure 5e. The digital photograph of the Zn-I$_2$ pouch battery with

View Article Online
DOI: 10.1039/D4EE05527F

skin-QSSE can be found in Figure S37. Pouch batteries exhibited an initial capacity of 119.0 mAh g^{-1} at 0.5 C and 99.9% CE for 300th cycle (Figure 5f), indicating excellent iodine retention by skin-QSSE. GCD curves implied that obvious discharging plateaus were maintained at 1st, 100th and 300th cycles (Figure 5g). The flexibility of Zn-I$_2$ pouch batteries with skin-QSSE was further examined by physical bending folding. No significant voltage fluctuations were observed after folding the pouches into 90° and 180°, and the voltage was maintained even after being cut (Figure 5h). Furthermore, series-connected pouch batteries with skin-QSSE provided stable power to a timer, further demonstrating their practicality (Figure 5i).

Material cost analysis of skin-QSSE is necessary to evaluate its prospects for large-scale energy storage applications. The commercial PPTA fibers have a lower cost, while the cost of skin-QSSE mainly comes from the DMSO and COF monomers (Table S2). As shown in Figure S38, the cost of skin-QSSE was calculated to be about 183.15 USD/m^2, which is lower than the commercial GF (284 USD/m^2) and Nafion (~1700 USD/m^2) used in LE. Considering the recyclability of the DMSO solvent and the scalable preparation process of skin-QSSE, its actual cost may not exceed its material cost. This cost analysis indicates that skin-QSSE is cost-competitive and has potential commercial viability.

Conclusions

In summary, inspired by the exquisite structure of human skin, we have designed an asymmetric skin-QSSE for ultra-durable Zn-I$_2$ batteries. Relying on the multifunctional structure of TFB-TAPT nanolayers and PPTA hydrogel in skin-QSSE, ionic migration behavior at the interface of anode and cathode was significantly improved. DFT calculations confirmed that the desolvation of hydrated Zn^{2+} was thermodynamically favorable in skin-QSSE (-0.66 eV of desolvation energy vs. 7.09 eV for LE), implying that the Zn-anode side reactions are weakened. From the MSD curves, the diffusion coefficient of Zn^{2+} ions (1.19 Å^2 ps^{-1}) were significantly higher than that of I$_3^-$ ions (0.14 Å^2 ps^{-1}) and I$^-$ ions (0.05 Å^2 ps^{-1}) in TFB-TAPT nano-channels, implying that polyiodide ions were selectively blocked. As a proof, the Zn–I$_2$ batteries with skin-QSSE exhibited a high specific capacity (201.5 mAh g^{-1}) at 0.5 C, prolonged cycling lifetime (45000 cycles) and superior capacity decay rate (0.0018‰) at 10 C. The remarkable improvement in electrochemical performance underlines the promise of the skin-QSSE strategy for advanced aqueous iodine-based energy storage systems.

Author contributions

Conceptualization, S.C.C.; Methodology, S.C.C., A.W.Z. and B.J.F; Investigation, S.C.C., Y.S.L., L.L.M. and W.Y.L.; Writing-Original Draft, S.C.C. and Y.S.L.; Writing-Review & Editing, S.C.C., Y.S.L., P.S.Y., S.H., Z.H.R., L.L.M. and W.Y.L.; Funding Acquisition, J.F.S.; Resources, J.F.S. and M.X.Y.; Supervision, J.F.S., M.X.Y. and H.Y.F.

Data availability

The data supporting this article have been included as part of the ESI.†

Conflicts of interest

There are no conflicts to declare.

Acknowledgements

This work was financially supported by the National Natural Science Foundation of China (52222315).

Notes and references

1. C. Xie, C. Wang, Y. Xu, T. Li, Q. Fu and X. J. N. E. Li, *Nat. Energy*, 2024, 1-11.
2. Y. Kang, G. Chen, H. Hua, M. Zhang, J. Yang, P. Lin, H. Yang, Z. Lv, Q. Wu, J. Zhao and Y. Yang, *Angew. Chem. Int. Ed.*, 2023, **62**, e202300418.
3. Y. Liang and Y. Yao, *Nat. Rev. Mater.*, 2023, **8**, 109-122.
4. L. Jiang, S. Han, Y.-C. Hu, Y. Yang, Y. Lu, Y.-C. Lu, J. Zhao, L. Chen and Y.-S. J. N. E. Hu, *Nat. Energy*, 2024, 1-10.
5. Y. Yuan, J. Yang, Z. Liu, R. Tan, M. Chuai, J. Sun, Y. Xu, X. Zheng, M. Wang, T. Ahmad, N. Chen, Z. Zhu, K. Li and W. Chen, *Adv. Energy Mater.*, 2022, **12**.
6. L. Su, F. Lu, Y. Li, Y. Wang, X. Li, L. Zheng and X. Gao, *ACS Nano*, 2024, DOI: 10.1021/acsnano.4c00593.
7. Z. Hou, Y. Gao, H. Tan and B. Zhang, *Nat Commun*, 2021, **12**, 3083.
8. D. Lin and Y. Li, *Adv. Mater.*, 2022, **34**.
9. W. Wang, C. Li, S. Liu, J. Zhang, D. Zhang, J. Du, Q. Zhang and Y. Yao, *Adv. Energy Mater.*, 2023, **13**.
10. G. Liang, B. Liang, A. Chen, J. Zhu, Q. Li, Z. Huang, X. Li, Y. Wang, X. Wang, B. Xiong, X. Jin, S. Bai, J. Fan and C. Zhi, *Nat Commun*, 2023, **14**, 1856.
11. K. K. Turekian and K. H. J. G. s. o. A. b. Wedepohl, *Geol. Soc. Am. Bull*, 1961, **72**, 175-192.
12. G. W. Meijer, G. Kanny and J. F. J. W. I. R.-R. Briois, *Wiley Interdisciplinary Reviews-RNA*, 2000.
13. L. Zhang, J. Huang, H. Guo, L. Ge, Z. Tian, M. Zhang, J. Wang, G. He, T. Liu, J. Hofkens, D. J. L. Brett and F. Lai, *Adv. Energy Mater.*, 2023, **13**.
14. X. Li, N. Li, Z. Huang, Z. Chen, G. Liang, Q. Yang, M. Li, Y. Zhao, L. Ma, B. Dong, Q. Huang, J. Fan and C. Zhi, *Adv. Mater.*, 2021, **33**.
15. Y. Kang, G. Chen, H. Hua, M. Zhang, J. Yang, P. Lin, H. Yang, Z. Lv, Q. Wu, J. Zhao and Y. Yang, *Angew. Chem. Int. Ed.*, 2023, **62**, e202300418.
16. Z. Hu, X. Wang, W. Du, Z. Zhang, Y. Tang, M. Ye, Y. Zhang, X. Liu, Z. Wen and C. C. Li, *ACS Nano*, 2023, **17**, 23207-23219.
17. X. Yang, H. Fan, F. Hu, S. Chen, K. Yan and L. Ma, *Nanomicro Lett*, 2023, **15**, 126.
18. L. Chai, X. Wang, Y. Hu, X. Li, S. Huang, J. Pan, J. Qian and X. Sun, *Adv. Sci.*, 2022, **9**, e2105063.
19. T. Geng, S. Ye, Z. Zhu and W. Zhang, *J. Mater. Chem. A*, 2018, **6**, 2808-2816.
20. J. Hu, Z. Zhang, T. Deng, F. C. Cui, X. Shi, Y. Tian and G. Zhu, *Adv Mater*, 2024, DOI: 10.1002/adma.202401091, e2401091.
21. Y. Zhao, Y. Wang, W. Xue, R. Cheng, X. Zheng, G. Zhu, D. Hu, H. Huang, C. Hu and D. Liu, *Adv. Mater.*, 2024, DOI: 10.1002/adma.202403097.
22. S. Huang, R. Tang, X. Liu, Y. Zhang, Y. Tang, Z. Wen, M. Ye, Y. Yang and C. C. Li, *Energy Environ. Sci.*, 2024, DOI: 10.1039/d3ee02945j.
23. F. Wang, W. Liang, X. Liu, T. Yin, Z. Chen, Z. Yan, F. Li, W. Liu, J. Lu, C. Yang and Q. H. Yang, *Adv. Energy Mater.*, 2024, DOI: 10.1002/aenm.202400110.

View Article Online
DOI: 10.1039/D4EE05527F

24. Y. Yang, S. Liang, B. Lu and J. Zhou, *Energy Environ. Sci.*, 2022, **15**, 1192-1200.
25. J. L. Yang, Z. Yu, J. Wu, J. Li, L. Chen, T. Xiao, T. Xiao, D. Q. Cai, K. Liu, P. Yang and H. J. Fan, *Adv. Mater.*, 2023, **35**, e2306531.
26. K. K. Sonigara, J. Zhao, H. K. Machhi, G. Cui and S. S. Soni, *Adv. Energy Mater.*, 2020, **10**.
27. F. Wu, Y. Ren, W. Lv, X. Liu, X. Wang, C. Wang, Z. Cao, J. Liu, J. Wei and Y. J. N. C. Pang, *Nat. Commun.*, 2024, **15**, 802.
28. B. Ying and X. Liu, *iScience*, 2021, **24**, 103174.
29. T. A. Harris-Tryon and E. A. Grice, *Science*, 2022, **376**, 940-945.
30. M. Wang, Y. Luo, T. Wang, C. Wan, L. Pan, S. Pan, K. He, A. Neo and X. Chen, *Adv. Mater.*, 2021, **33**, 2003014.
31. J. Zhu, M. Yang, A. Emre, J. H. Bahng, L. Xu, J. Yeom, B. Yeom, Y. Kim, K. Johnson, P. Green and N. A. Kotov, *Angew. Chem. Int. Ed.*, 2017, **56**, 11744-11748.
32. Y. Yang, H. Hua, Z. Lv, W. Meng, M. Zhang, H. Li, P. Lin, J. Yang, G. Chen, Y. Kang, Z. Wen, J. Zhao and C. C. Li, *ACS Energy Lett.*, 2023, **8**, 1959-1968.
33. S. Cao, J. Tan, L. Ma, Y. Liu, Q. He, W. Lu, Z. Liu, M. Ye and J. Shen, *Energy Stor. Mater.*, 2024, **66**, 103232.
34. A. Knebel and J. Caro, *Nat. Nanotechnol.*, 2022, **17**, 911-923.
35. C. Kang, Z. Zhang, V. Wee, A. K. Usadi, D. C. Calabro, L. S. Baugh, S. Wang, Y. Wang and D. Zhao, *J. Am. Chem. Soc.*, 2020, **142**, 12995-13002.
36. A. Zhang, J. Zhu, S. Han, Y. Zhang and B. Van der Bruggen, *J. Membr. Sci.*, 2022, **662**, 120987.
37. T. Wei, L. e. Mo, Y. Ren, H. Zhang, M. Wang, Y. He, P. Tan, Z. Li, W. Chen and L. Hu, *Energy Stor. Mater.*, 2024, **70**, 103525.
38. J. Xu, S. An, X. Song, Y. Cao, N. Wang, X. Qiu, Y. Zhang, J. Chen, X. Duan, J. Huang, W. Li and Y. Wang, *Adv. Mater.*, 2021, **33**, 2105178.
39. X. Kong, Z. Wu, M. Stromme and C. Xu, *J Am Chem Soc*, 2024, **146**, 742-751.
40. L. Bai, Q. Gao and Y. Zhao, *J. Mater. Chem. A*, 2016, **4**, 14106-14110.
41. X. Zhao, Q. Li, P. Pachfule, Z. Wang, S. Liu, W. Wu, M. Wu and A. Thomas, *Small*, 2023, **19**, 2301200.
42. Z. Mu, Y. Zhu, Y. Zhang, A. Dong, C. Xing, Z. Niu, B. Wang and X. Feng, *Angew. Chem. Int. Ed.*, 2023, **62**, e202300373.
43. Y.-N. Lu, K. Mo, X.-H. Liang, J.-S. Xie, Y. Yang, L. Zheng, M. Gu, X.-R. Liu, Y. Lu and J. Ge, *ACS Appl. Mater. Interfaces*, 2024, **16**, 60992-61003.
44. S. Yang, Y. Zhang, Y. Zhang, J. Deng, N. Chen, S. Xie, Y. Ma and Z. Wang, *Adv. Funct. Mater.*, 2023, **33**.
45. P. Lin, G. Chen, Y. Kang, M. Zhang, J. Yang, Z. Lv, Y. Yang and J. Zhao, *ACS Nano*, 2023, **17**, 15492-15503.
46. K. Zhu, L. Wu, C. Guo, J. Pu, Y. Liu, X. Chen, Y. Chen, P. Xue, J. Han and Y. Yao, *Adv. Funct. Mater.*, 2023, **33**.
47. J. L. Yang, T. Xiao, T. Xiao, J. Li, Z. Yu, K. Liu, P. Yang and H. J. Fan, *Adv. Mater.*, 2024, DOI: 10.1002/adma.202313610, e2313610.
48. M. Li, Z. Li, X. Wang, J. Meng, X. Liu, B. Wu, C. Han and L. Mai, *Energy Environ. Sci.*, 2021, **14**, 3796-3839.
49. C. Guo, Y. Cao, Y. Gao, C. Zhi, Y. X. Wang, Y. Luo, X. J. Yang and X. Luo, *Adv. Funct. Mater.*, 2024, DOI: 10.1002/adfm.202314189.
50. Y. Su, X. Wang, M. Zhang, H. Guo, H. Sun, G. Huang, D. Liu and G. Zhu, *Angew. Chem. Int. Ed.*, 2023, **62**, e202308182.
51. H. Xu, R. Zhang, D. Luo, J. Wang, H. Dou, X. Zhang and G. Sun, *ACS Nano*, 2023, **17**, 25291-25300.
52. J. L. Yang, H. H. Liu, X. X. Zhao, X. Y. Zhang, K. Y. Zhang, M. Y. Ma, Z. Y. Gu, J. M. Cao and X. L. Wu, *J Am Chem Soc*, 2024, DOI: 10.1021/jacs.3c12638.
53. L. Yang, Y. J. Zhu, H. P. Yu, Z. Y. Wang, L. Cheng, D. D. Li, J. Tao, G. He and H. Li, *Adv. Energy Mater.*, 2024, DOI: 10.1002/aenm.202401858.
54. X. Li, J. Yu, W. Li, Y. Liao, M. Li, B. Zhao, X. Liu, S. Huang, S. Xia, J. Zhang and Y. Jiang, *Chem. Eng. J.*, 2025, **505**, 159355.
55. M. Wang, Y. Meng, M. Sajid, Z. Xie, P. Tong, Z. Ma, K. Zhang, D. Shen, R. Luo, L. Song, L. Wu, X. Zheng, X. Li and W. Chen, 2024, **63**, e202404784.
56. X. Li, Y. Wang, Z. Chen, P. Li, G. Liang, Z. Huang, Q. Yang, A. Chen, H. Cui, B. Dong, H. He and C. Zhi, 2022, **61**, e202113576.
57. H. Wang, X. Liu, J. Zhong, L. Du, S. Yun, X. Zhang, Y. Gao and L. Kang, *Small*, 2024, **20**, 2306947.

View Article Online
DOI: 10.1039/D4EE05527F

The data supporting the findings of this study are included within the main article and the ESI.